

Construction of Pixel-Level Resolution DEMs from Monocular Images by Shape and Albedo from Shading Constrained with Low-Resolution DEM

Bo Wu^a, Wai Chung Liu^a, Arne Grumpe^b, Christian Wöhler^b

^a Department of Land Surveying and Geo-Informatics, The Hong Kong Polytechnic University, Hung Hom, Hong Kong

^b Image Analysis Group, TU Dortmund, 44227 Dortmund, Germany

Corresponding author:

Bo Wu, Ph.D.

Associate Professor

Department of Land Surveying and Geo-Informatics

Hong Kong Polytechnic University

Hung Hom, Kowloon, Hong Kong

Tel: +852 2766 4335 Fax: +852 2330 2994

Email: bo.wu@polyu.edu.hk

Abstract:

Lunar Digital Elevation Model (DEM) is important for lunar successful landing and exploration missions. Lunar DEMs are typically generated by photogrammetry or laser altimetry approaches. Photogrammetric methods require multiple stereo images of the region of interest and it may not be applicable in cases where stereo coverage is not available. In contrast, reflectance based shape reconstruction techniques, such as shape from shading (SfS) and shape and albedo from shading (SAfS), apply monocular images to generate DEMs with pixel-level resolution. We present a novel hierarchical SAfS method that refines a lower-resolution DEM to pixel-level resolution given a monocular image with known light source. We also estimate the corresponding pixel-wise albedo map in the process and based on that to regularize the shape reconstruction with pixel-level resolution based on the low-resolution DEM. In this study, a Lunar-Lambertian reflectance model is applied to estimate the albedo map. Experiments were carried out using monocular images from the Lunar Reconnaissance Orbiter Narrow Angle Camera (LRO NAC), with spatial resolution of 0.5 to 1.5 meters per pixel, constrained by the Selenological and Engineering Explorer and LRO Elevation Model (SLDEM), with spatial resolution of 60 meters. The results indicate that local details are well recovered by the proposed algorithm with plausible albedo estimation. The low-frequency topographic consistency depends on the quality of low-resolution DEM and the resolution difference between the image and the low-resolution DEM.

Keywords: Moon, DEM, Shape and Albedo from Shading, Monocular Image, LRO NAC

1. Introduction

Lunar digital elevation models (DEMs) are generally obtained from stereo photogrammetry or laser altimetry (Smith et al., 2010; Wu et al., 2014a). Stereo photogrammetric processing requires coverage of a target area with stereo images and is able to produce DEMs with resolutions of about three times the image resolution (Zhu et al., 2010). Photogrammetry focuses mainly on the imaging geometry, and the image photometric content is often used for conjugate matching. Although stereo coverage is a prerequisite, for some lunar orbiter cameras such as the Lunar Reconnaissance Orbiter Narrow Angle Camera (LRO NAC), high-resolution stereo availability is limited due to its orbital and mission design (Tran et al., 2010), which hinders the production of high-resolution DEMs by stereo photogrammetry. Laser altimetry, such as with the Lunar Orbiter Laser Altimeter (LOLA; Smith et al., 2010), produces highly reliable global topographic information of the Moon for various scientific purposes. However, it is also characterized by its large sample spacing, resulting in low-resolution DEMs (e.g., 1024 pixels per degree for LOLA DEMs), and the use of derived topographic products for high-resolution purposes may introduce significant interpolation artifacts that limit its applications (Wu et al., 2014b).

Reflectance-based surface reconstruction methods such as shape from shading (SfS) and shape and albedo from shading (SAfS) estimate the three-dimensional (3D) surface shape solely on the basis of image photometric content such as intensity values. Such methods use the information captured in every pixel of one or more image(s) and reconstruct them on the resulting topography. Apart from drawbacks of instability and solution ambiguity, reflectance-based surface reconstruction methods show potential as a complement to the existing DEM production methods (i.e., stereo photogrammetry and laser altimetry), which are reliable and accurate on large scales (Kirk et al., 2003). The relatively simple surface

albedo complexity of major planetary bodies of interest also favors the use of such techniques in lunar and planetary mapping.

In this paper, a novel hierarchical SAfS method is presented that refines an existing low-resolution DEM (either from laser altimetry data or stereo photogrammetry) to image pixel-level resolution by reflectance-based surface reconstruction techniques using a single image. Section 2 summarizes other studies related to the topic, and Section 3 describes the details of the approach. The experimental results using LRO NAC imagery with spatial resolution of 0.5 to 1.5 meters per pixel, constrained by the Selenological and Engineering Explorer and LRO Elevation Model (SLDEM) with spatial resolution of 60 meters are presented in Section 4, and Section 5 provides a brief discussion and the concluding remarks.

2. Related Work

Reflectance-based surface reconstruction (e.g., SfS) has been extensively studied for more than half a century (Kirk et al., 2003) and was presented and mathematically detailed by Horn (1977, 1990). Using only the intensity information of the image(s), these methods recover the surface slopes and heights along the direction of illumination (Horn, 1977). The assumption is made that, among all combinations of slope and aspect, the slope along the illumination direction has the dominant effect on the resulting image reflectance. This one-dimensional (profile-based) reconstruction technique is called photoclinometry. A two-dimensional surface is photoclinometrically reconstructed by combining adjacent reconstructed characteristic stripes. Profile-based construction would present visible inconsistencies between adjacent stripes because the control over the geometry of the surface and the variations in the reflecting ability of the surface material is less comprehensive. There are algorithms that address the problem by means of a filter over the resulting surface (Kirk et

al., 2003). SfS can be seen as an extended version of photoclinometry, but instead of reconstructing the profiles (one-dimensional) that control the aspect to face the sun, SfS algorithms usually work on small surface patches for which two-dimensional information is considered and solved for both slope and aspect. SfS algorithms provide better geometric consistency, but they have greater solution ambiguity, so regularization is needed. Later developments allowed photoclinometry to overcome stripe inconsistencies, and the difference between photoclinometry and SfS has become much less distinct (Grumpe et al., 2014).

Reflectance-based reconstruction has been intensively studied in computer vision for close-range scene reconstruction applications (Chandraker et al., 2007; Barron and Malik, 2012; Wang et al., 2016), for which SfS is considered as a specific intrinsic image decomposition problem (Barron and Malik, 2012). It was originally proposed for lunar and planetary mapping (Horn, 1990), and systematic analysis was performed for remote sensing and planetary mapping applications (Piechullek and Heipke, 1996; Piechullek et al., 1998; Lohse and Heipke, 2004). In these works, multiple remote-sensing images were used to generate the terrain model for an area; these images had different illumination conditions, so sufficient constraints were available. The results show the possible utility of SfS as an alternative for generation of high-resolution topographic models.

The performance and results of reflectance-based algorithms are greatly affected by the reflecting ability of the surface, which is loosely termed albedo. Albedo varies locally, so simultaneous estimation of the local albedo and the shape is mathematically ill-posed. Some algorithms avoid this problem by assuming albedo with certain constants (Horn, 1990; Lohse and Heipke, 2004). Other algorithms attempt to solve for both shape and locally varying albedo (i.e., SAfS). SAfS can be achieved with multiple images or a single image. Multiple images with different illumination conditions (photometric stereo) provide sufficient or redundant conditions for estimation of both shape and albedo (Woodham, 1980; Chandraker

et al., 2007); however, this implies that sufficient photometric stereo sets of the target are required, thus limiting its availability and applicability. In contrast, SAfS of a single image provides much greater availability because no excess images are needed, whereas its severely under-constrained situation requires regularization and assumption to produce a desirable solution. Approaches to overcome the under-constrained situation include data training and machine learning (Barron and Malik, 2011) and separation of the albedo and shape optimization routines (Danzl and Scherer, 2002; Grumpe et al., 2014).

The incorporation of existing low-resolution DEMs into SAfS algorithms using single or multiple images combines the geometric accuracy of low-resolution DEMs and the pixel-level reconstruction ability of SAfS. Algorithms have been explored and developed (Barron and Malik, 2012; Grumpe et al., 2014) with promising results. A low-resolution DEM provides a constraint over shape geometry and encourages the resulting DEM from SAfS to comply with the general geometry of the low-resolution DEM.

For remote sensing and planetary mapping applications, SAfS based on monocular images combined with low-resolution DEM algorithms can be found in Barron and Malik (2011; 2012). In these works, the albedo parameter is written as a function of shape and is optimized toward certain statistical properties; thus, the method is viewed as a combined approach (to estimate both shape and albedo in the same routine). This technique produces a visually reliable and detailed model from a low-resolution DEM. However, it requires training datasets, which limits its application. There have been no detailed examinations of the resulting DEM, and follow-up studies of this approach for planetary remote sensing are nearly absent. Conclusions about its application in planetary remote sensing cannot be drawn.

Another algorithm (Danzl and Scherer, 2002; Grumpe et al., 2014) separates shape and albedo and optimizes them alternately. The shape is constrained by the input low-resolution DEM, and its albedo is optimized by a low-pass algorithm with decreasing

width to obtain low-frequency information. These works produce stable and decent results with more in-depth analysis and comparisons. The resulting albedo may require inspection to ensure that topographic details (i.e., shading) do not exist, and optimization over albedo must be terminated once shading is apparent in the resulting albedo.

3. SAfS Constrained by Low-Resolution DEM

3.1 Framework of the Approach

The framework of the proposed method is outlined in Figure 1. We first assume a known light source and a known viewer position so that only the surface heights (i.e., shape) are unknown. Pixel-wise albedo estimation is included in the optimization framework so that the resulting shape corresponds to a plausible albedo. The algorithm adopts an iterative hierarchical structure starting from the lowest predefined resolution, which is a factor of the resolution of the input coarse DEM, and then increases the resolution by a factor of two until it approaches the image's pixel resolution. The process is initialized in the initial hierarchy step and iterated and optimized in the iterative hierarchy step, and finally a refined pixel-level resolution DEM is produced and its corresponding albedo is derived.

With a low-resolution DEM as input, the initial hierarchy derives an up-sampled DEM by a factor of two, and resamples the image to unify the resolution with the DEM. The resampled DEM and image are then forwarded to a multiple-grid SAfS algorithm together with the input low-resolution DEM and the corresponding down-sampled image (with the same resolution with the former). The multiple-grid SAfS algorithm optimizes the up-sampled DEM with respect to the recorded image intensity and terrain geometry. A multiple-grid structure possesses better convergence properties (Horn, 1990) and allows

interactions between multiple resolutions. The optimization result of the lower-resolution data is transferred to the higher-resolution data via an interpolation relationship followed by optimization of the higher-resolution data. The result from the higher-resolution optimization is then back-propagated to its low-resolution counterpart by down-sampling. At this step, the interaction between the low-resolution components (i.e., the low-resolution DEM and the low-resolution image) and the higher-resolution components (i.e., resolution of the current hierarchy) is established; such interactions allow optimization of both the low-resolution DEM and the refined SAfS DEM, which ensures a high degree of geometric correspondence between the two resolutions without over-constraining the final output.

The iterative hierarchy takes the refined SAfS DEM as input, up-samples it by a factor of two, and forwards the up-sampled DEM to the multiple-grid SAfS algorithm with other inputs similar to the initial hierarchy. The refined DEM is taken as input for the next iteration, and the same processes are performed until the DEM reaches the same resolution as the image. The final refined pixel-level resolution DEM is then exported as the output of the SAfS algorithm, and its corresponding albedo is derived from the refined pixel-level resolution DEM and the original image.

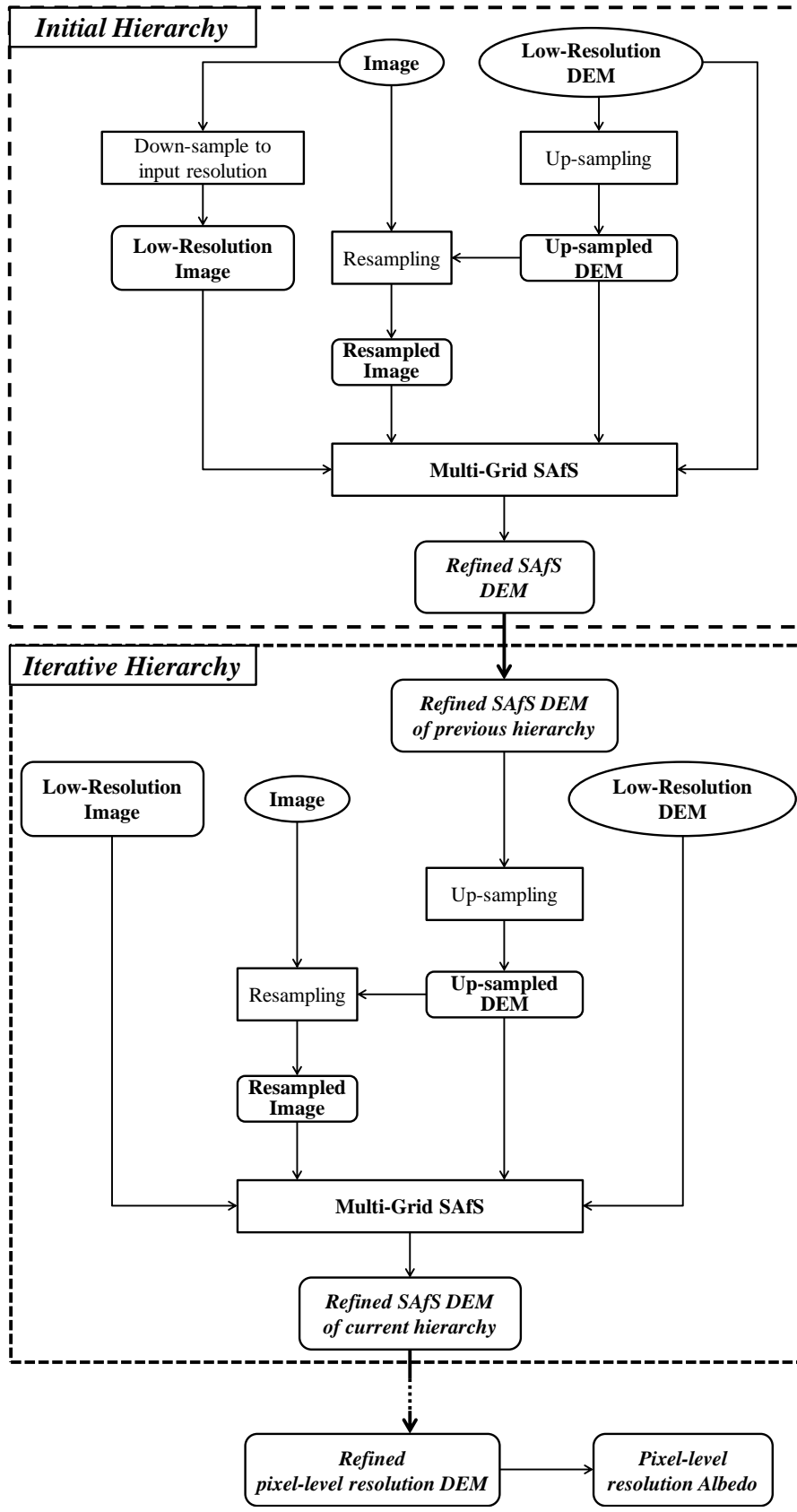


Fig. 1 Framework of the hierarchical SAfS algorithm.

3.2 Reflectance Model

The relationship between the photometric image content and shape can be written as

$$I = A \times G(p, q) \quad (1)$$

Equation 1 describes the relationship between the resulting image intensity I , the surface reflecting properties (i.e., albedo, A), and the reflectance $G(p, q)$ produced by shape. The reflectance and albedo can be expressed as the ratio of the incoming energy of a location to its reflected energy captured by a sensing system due to surface material properties and its geometry; therefore, these ratios cannot be negative, nor can they exceed unity. The reflectance model $G(p, q)$ defines the relationship between the image intensity I and the shape (3D topography). The model relates the surface normal (p, q) , the illumination conditions, and the energy to be reflected to the sensor (i.e., the image intensity). Various models can be used depending on the applications and data, such as the sophisticated Hapke model (Hapke, 2002; Hapke, 2012) if measurements in physical units are available (Grumpe et al., 2014) or the empirical lunar–Lambert model (McEwen, 1991) if only image intensities are available. In this study, the lunar–Lambert model is used, as described in equation (2):

$$G(p, q) = (1 - \lambda) \cos i(p, q) + 2\lambda \frac{\cos i(p, q)}{\cos i(p, q) + \cos e(p, q)} \quad (2)$$

where $i(p, q)$ is the incidence angle between the surface normal (p, q) and the solar ray and $e(p, q)$ is the emission angle between the surface normal and the sensor. The lunar–Lambert model is a combination of the Lambertian model and the Lommel-Seeliger law with the term λ controlling their weights. λ is a function of phase angle (i.e., the angle between incidence vector and emission vector) and can be modelled by a 3rd-order polynomial function described in Lohse et al. (2006).

3.3 Shape Reconstruction Constrained by Low-Resolution DEM

Reflectance-based shape recovery consists of two steps. The first step estimates the surface normal (i.e., negative surface gradients) from the reflectance values and the other estimates the shape (i.e., actual height values) from the surface normal. Reflectance-based shape recovery from raw images also includes a step in which the reflectance (shading information) is estimated from the image intensity, which usually contains noise and variations in albedo. Therefore, a SAfS algorithm can be explained in three main components: (1) reflectance and albedo from image intensity; (2) gradients from reflectance; and (3) height from gradients. Within each of these components, the contribution of the low-resolution DEM is to encourage the process to converge to a solution close to the low-resolution DEM without neglecting local topographic details recoverable from the image.

3.3.1 Reflectance and Albedo from Image Intensity

The reflectance $G(p,q)$ is the only connection between shape and image intensity, and it is embedded in the image intensity value I as described in equation (1). This relationship contains another unknown — the albedo A . Because the albedo and reflectance are related by equation (1), estimation of a plausible reflectance implies a reasonable albedo; therefore, the derivation of desirable reflectance with albedo considerations is introduced. With only one image, it is mathematically impossible to solve for both unknowns in one observation unless additional information is provided, such as assumptions (Horn, 1990; Kirk et al., 2003) or statistical results from other studies (Barron and Malik, 2011). In this study, it is assumed that the albedo of a location would be highly similar to its close vicinity, yielding the “local-constant albedo assumption”. This assumption is logical and has been adopted in

various studies (Lee and Rosenfeld, 1983; Tsai and Shah, 1998; Grumpe et al., 2014) for both close-range scenes and planetary mapping. With this assumption, the reflectance of a location (x,y) can be estimated by relating it to its surrounding pixels, yielding a linear system of equations:

$$\frac{A_{x,y}}{A_{i,j}G_{i,j}}G_{x,y} = \frac{I_{x,y}}{I_{i,j}} \quad (3)$$

where $G_{x,y}$ and $I_{x,y}$ are the reflectance value and the image intensity of the current location (x,y) . $G_{i,j}$ and $I_{i,j}$ are the reflectance value and the image intensity of the surrounding location (i,j) .

A set of equation (3), one for each valid vicinity (i,j) , forms a linear system where $G_{x,y}$ is the unknown to be solved by the least-squares approach, and therefore no initial value is required for $G_{x,y}$, whereas $G_{i,j}$ are computed from the existing gradient fields and $I_{x,y}$ and $I_{i,j}$ are extracted from the image. The albedo A is assumed to be locally constant; therefore, $A_{x,y} = A_{i,j}$ in the algorithm. Dividing $I_{x,y}$ by $I_{i,j}$ largely reduces the influence of albedo, leaving the reflectance value to be solved.

Because both albedo and reflectance are ratios of energy reflection, they cannot exceed unity, assuming that every pixel on the image is illuminated and can be viewed by the sensor (i.e., it has a positive value regardless of noise). Both the albedo and the reflectance must be greater than zero. By rearranging equation (1), albedo and reflectance can be expressed by each other, and thus their limits can be estimated:

$$\begin{aligned} \therefore 0 < A = \frac{I}{G} \leq 1 \quad \text{and} \quad 0 < G = \frac{I}{A} \leq 1 \\ \therefore 0 < I \leq G \leq 1 \quad \text{and} \quad 0 < I \leq A \leq 1 \end{aligned} \quad (4)$$

Equation (4) suggests that feasible albedo and reflectance must be at least equal to the image intensity value, regardless of noise. The reflectance estimated by equation (3) is constrained so that it will not exceed the feasible range suggested by equation (4), and as a result, its corresponding albedo will also be within a valid range.

3.3.2 Gradients from Reflectance

Given any reflectance value (G), the SAFS algorithm estimates a corresponding surface normal, which is the negative of the surface gradients and is defined as:

$$\begin{bmatrix} p \\ q \end{bmatrix} = \begin{bmatrix} -\frac{\partial z}{\partial L} \\ -\frac{\partial z}{\partial T} \end{bmatrix} \quad (5)$$

where p is the surface normal along illumination direction (L) and q is the surface normal perpendicular to illumination direction (T). This can be estimated by using finite difference discretization over a small patch of the surface. A 2×2 surface patch from the DEM is extracted, and the following convolution equation is applied over the extracted patch to obtain an estimated surface normal along the horizontal (x) and vertical directions (y):

$$\begin{bmatrix} -\frac{\partial z}{\partial x} \\ -\frac{\partial z}{\partial y} \end{bmatrix} = \begin{bmatrix} \sum \begin{bmatrix} 1 & -1 \\ 1 & -1 \end{bmatrix} \frac{1}{2h_x} \circ \begin{bmatrix} Z_{x,y+1} & Z_{x+1,y+1} \\ Z_{x,y} & Z_{x+1,y} \end{bmatrix} \\ \sum \begin{bmatrix} -1 & -1 \\ 1 & 1 \end{bmatrix} \frac{1}{2h_y} \circ \begin{bmatrix} Z_{x,y+1} & Z_{x+1,y+1} \\ Z_{x,y} & Z_{x+1,y} \end{bmatrix} \end{bmatrix} \quad (6)$$

where h_x and h_y are the cell size in horizontal and vertical directions; and

$[*] \circ [*]$ is the element-wise multiplication. It is then projected to the illumination direction and the illumination normal direction by:

$$\begin{aligned} p &= \begin{bmatrix} -\frac{\partial z}{\partial x} & -\frac{\partial z}{\partial y} \end{bmatrix} \begin{bmatrix} x_L & y_L \end{bmatrix}^T \left(\frac{1}{\sqrt{(p_L^2 + q_L^2)}} \right) \\ q &= \begin{bmatrix} -\frac{\partial z}{\partial x} & -\frac{\partial z}{\partial y} \end{bmatrix} \begin{bmatrix} x_T & y_T \end{bmatrix}^T \left(\frac{1}{\sqrt{(p_T^2 + q_T^2)}} \right) \end{aligned} \quad (7)$$

where the illumination vector is defined by $\begin{bmatrix} x_L \\ y_L \end{bmatrix}$ and the illumination normal is defined by $\begin{bmatrix} x_T \\ y_T \end{bmatrix}$.

The relationship between the reflectance (G) and surface normal $\begin{bmatrix} p \\ q \end{bmatrix}$ is described in

equation (2), and thus the function gradients, notably $\left(\frac{\partial G}{\partial p} \quad \frac{\partial G}{\partial q}\right)$, can be computed mathematically by finite differences. Given an estimated reflectance value (G_E), the reflectance cost function which is the core component of the SAfS algorithm, can be formed and linearized as:

$$(G_0|_{DEM}) + \left(\frac{\partial G}{\partial p}\right)|_{DEM} \Delta p + \left(\frac{\partial G}{\partial q}\right)|_{DEM} \Delta q = G_E \quad (8)$$

where G_0 is referred to as the initial reflectance value; $\left(\frac{\partial G}{\partial p} \quad \frac{\partial G}{\partial q}\right)$ are the derivatives with respect to surface normal p and q ; and G_E is the estimated reflectance. As suggested by Horn (1990) and adopted by Grumpe et al. (2014), the initial reflectance and its function gradients are evaluated at the surface normal of the current DEM.

Because there is only one reflectance observation and two unknowns, the system is underdetermined. Therefore, the strategy by Horn (1990) that includes the integrability constraints into computation is adopted. Integrability ensures that for all possible routes between two points on the gradient field (i.e., surface gradient map), the accumulated height difference between the two points for each route will always be the same. The integrability constraint by Horn (1990) can be expressed as searching for a solution that is closest to the surface normal of the current DEM, which is also similar to the idea expressed by Frankot and Chellappa (1988), yielding the cost function:

$$F = (p - p_{DEM})^2 + (q - q_{DEM})^2 \quad (9)$$

where $\begin{bmatrix} p_{DEM} \\ q_{DEM} \end{bmatrix}$ are the surface normal of the current SAfS DEM along and perpendicular to the direction of illumination.

If the low-resolution gradient map is resampled from the current gradient map by certain down-sampling methods, the residuals between the down-sampled gradients and the reference low-resolution gradients of the current iteration can then be estimated, yielding a cost function as:

$$\begin{aligned}
F &= (p - p_{DEM})^2 + (q - q_{DEM})^2 + w_{coarse} \left[p - (\bar{p}_0 + \Delta p_{SAfS}|_{coarse}) \right]^2 \\
&\quad + w_{coarse} \left[q - (\bar{q}_0 + \Delta q_{SAfS}|_{coarse}) \right]^2 \\
\Delta p_{SAfS}|_{coarse} &= p_{SAfS}|_{coarse} - p_{coarse} \\
\Delta q_{SAfS}|_{coarse} &= q_{SAfS}|_{coarse} - q_{coarse}
\end{aligned} \tag{10}$$

where $\begin{bmatrix} p_{coarse} \\ q_{coarse} \end{bmatrix}$ is the surface normal from the down-sampled DEM at current iteration; $\begin{bmatrix} p_{SAfS}|_{coarse} \\ q_{SAfS}|_{coarse} \end{bmatrix}$ is the surface normal of from the DEM optimized by SAfS; it is initialized by SAfS optimization at low-resolution level and is updated per iteration through the module ‘Low-resolution SAfS’ in the multi-gridding architecture. Further details will be discussed in section 3.4. \bar{p}_0 and \bar{q}_0 are the local mean of the initial estimate of the surface normal; and w_{coarse} is the weight to control the effect of low-resolution DEM involvement.

For each node (x,y) , its low-resolution surface normal $\begin{bmatrix} p_{coarse} \\ q_{coarse} \end{bmatrix}$ and $\begin{bmatrix} p_{SAfS}|_{coarse} \\ q_{SAfS}|_{coarse} \end{bmatrix}$ is chosen by the nearest neighbor which can be shown experimentally to be sufficient to take low-resolution DEM into account effectively. The resampling processes between hierarchies produce interpolation artifacts of the initial gradient fields at the start of the first iteration, and therefore a smoothness term similar to other works is added (Horn, 1990; Danzl and Scherer, 2002) to reduce interpolation errors. This term, however, is artificial (Grumpe et al., 2014), which might smooth out possible details; this situation is refrained by the optimization strategy described as follows.

The optimization combines equations (8) and (10). Equation (8) describes the energy reflecting ratio, and equation (10) describes the negative tangent of the geometry, so

normalization and weighting would be essential to ensure a balance between the constraints. Such considerations are partially refrained by setting one constraint as absolute and the other as approximate and to be minimized, which corresponds to minimizing equation (10) subject to equation (8). This strategy ensures the effect of the reflectance constraint that the resulting surface normal must comply. The newly computed surface normal is not perfectly integrable due to albedo inaccuracies, image noise, and other geometric ambiguities, and will be corrected during the next step of height estimation.

3.3.3 Height from Gradients

‘Height from gradients’ directly recovers the height values of the DEM grid nodes with the newly computed surface normal. The relationship between a surface normal and its member node heights is described by equations (6) and (7). The optimization adjusts one node at a time so that its related set of surface normals, as illustrated in Figure 2, complies with the estimated surface normal from SAfS, yielding the equation (11):

$$\begin{bmatrix} p_{DEM} \\ q_{DEM} \end{bmatrix}_{i,j} + \begin{bmatrix} \frac{\partial p_{DEM}}{\partial Z_{x,y}} \\ \frac{\partial q_{DEM}}{\partial Z_{x,y}} \end{bmatrix}_{i,j} \Delta Z_{x,y} = \begin{bmatrix} p_{SAfS} \\ q_{SAfS} \end{bmatrix}_{i,j} + \begin{bmatrix} \Delta p_{SAfS}|_{coarse} \\ \Delta q_{SAfS}|_{coarse} \end{bmatrix}_{x,y} \quad (11)$$

where $\begin{bmatrix} p_{DEM} \\ q_{DEM} \end{bmatrix}_{i,j}$ and $\begin{bmatrix} p_{SAfS} \\ q_{SAfS} \end{bmatrix}_{i,j}$ are the surface normal of the current DEM and those estimated by SAfS at location (i,j) , respectively;

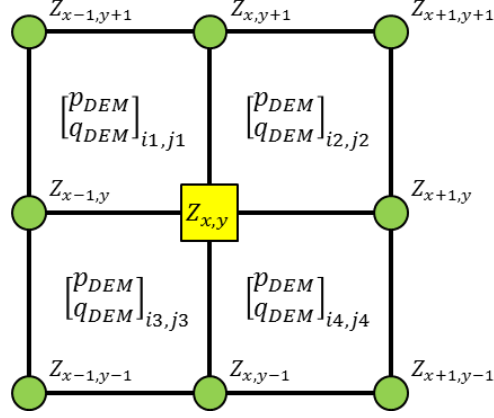


Fig. 2 Related surface normals of a grid node.

For each location (i,j) , an individual equation (11) is constructed. They form a linear system with $\Delta Z_{x,y}$ as the only unknown; this linear system is over-determined and thus a least-squares solution is obtained. The optimization can be viewed as a search for the integrable surface closest to the estimated set of the surface normals, which might not be

integrable, resulting from the SAfS algorithm. The term $\begin{bmatrix} \Delta p_{SAfS}|_{coarse} \\ \Delta q_{SAfS}|_{coarse} \end{bmatrix}_{x,y}$ is added into the

adjustment to account for the residual between the estimated gradient field from SAfS and the reference low-resolution DEM. This error term is evaluated at the center location (x,y) and is applied to all neighbor (i,j) to preserve the relative difference of the surface normal.

A direct introduction of the height values of the reference low-resolution DEM into SAfS as absolute height constraint is not considered in our algorithm, because such a constraint largely hinders detailed shape reconstruction at the early stages of the hierarchy (i.e., lower-resolution stages). This situation exists because, for certain locations, the reference low-resolution DEM is unable to capture key topographic characteristics at its effective resolution, which leads to over-flattening of the resulting SAfS DEM.

For boundary nodes for which not all neighboring surface normals are available, the optimization only considers neighbors for which a surface normal is available, which is equivalent to reducing the number of equations in the least-squares linear system. However, because each surface normal contains two equations, namely p and q , the resulting $Z_{x,y}$ would always be a least-squared solution even if only one surface normal is available.

3.4. Hierarchical Optimization

The optimization performs the SAfS process in a hierarchical structure: the lower resolutions (i.e., half the input DEM resolution) are processed first, and their results are up-sampled for the next pyramid level. The Gauss-Seidel relaxation scheme is adopted to optimize the surface normal and its subsequent surface heights one by one. This scheme is characterized by sequential updating of data (Horn, 1990) as opposed to the Jacobi scheme and exhibits the importance of the data processing sequence, which might introduce systematic noise into the results. The update sequence used in this study is related to the illumination direction, and more than one sequence are used in the process; therefore, several loops, one for each predefined sequence, are included in one complete iteration.

The SAfS algorithm contains three steps: (1) reflectance and albedo from image intensity that estimates the albedo-concerned reflectance from a single image; (2) gradients from reflectance that recover the surface normal from reflectance; and (3) the height from the gradients, which reconstructs the underlying surface heights from the surface normal. The module ‘gradients from reflectance’ is an underdetermined system in which two unknowns (i.e., p and q) are solved with one observation (i.e., the reflectance). Therefore, the observation is set to be absolute, and minimization of the integrability error subject to the reflectance observation is performed. This is solved with Lagrange multipliers, which is a

conventional technique for optimization of such problems.

The workflow of the multiple-grid SAfS algorithm is illustrated in Figure 3. The algorithm takes the image and the higher-resolution DEM (i.e., the resolution of the current hierarchy) and their low-resolution counterparts (i.e., the resolution of the initial low-resolution DEM) as inputs and performs SAfS on both resolutions, namely, the current-resolution SAfS and the low-resolution SAfS, within one routine. The algorithm starts with the current-resolution SAfS, which optimizes the higher-resolution DEM according to the image via the aforementioned steps of reflectance and albedo from image intensity and gradients from reflectance; the two steps produce a surface normal field that might not be integrable. This surface normal field is then resampled to the same low resolution (coarse surface normal map in Figure 3), which becomes $\begin{bmatrix} p_{coarse} \\ q_{coarse} \end{bmatrix}$ in equation (10) and is forwarded to the low-resolution SAfS process. The low-resolution SAfS process undergoes the entire routine of reflectance and albedo from image intensity, gradients from reflectance, and height from gradients at the low-resolution level. The resulting optimized surface normal (coarse SAfS surface normal map in Figure 3), expressed as $\begin{bmatrix} p_{SAfS} \\ q_{SAfS} \end{bmatrix}_{coarse}$ in equation (10), is then imported back into the current-resolution SfS module. The refined SAfS DEM is produced through ‘Height from gradients’, whereas the albedo is generated from the refined SAfS DEM.

Slightly different from equation (10), which is used in the current-resolution SAfS for gradient from reflectance, the cost function used in the low-resolution SAfS takes both the down-sampled results of SAfS (i.e., $\begin{bmatrix} p_{coarse} \\ q_{coarse} \end{bmatrix}$) and those of the input low-resolution DEM into account, yielding another cost function:

$$F = \left(p_{SAfS}|_{coarse} - p_{Ref} \right)^2 + \left(q_{SAfS}|_{coarse} - q_{Ref} \right)^2 + w_{coarse} \left(p_{SAfS}|_{coarse} - p_{coarse} \right)^2 + w_{coarse} \left(q_{SAfS}|_{coarse} - q_{coarse} \right)^2 \quad (12)$$

where $\begin{bmatrix} p_{coarse} \\ q_{coarse} \end{bmatrix}$ is the coarse surface normal as a down-sampled result of the current-resolution SAfS process; $\begin{bmatrix} p_{Ref} \\ q_{Ref} \end{bmatrix}$ is the surface normal of the input reference low-resolution DEM; and w_{coarse} is the weight to control the influence of the down-sampled surface normal.

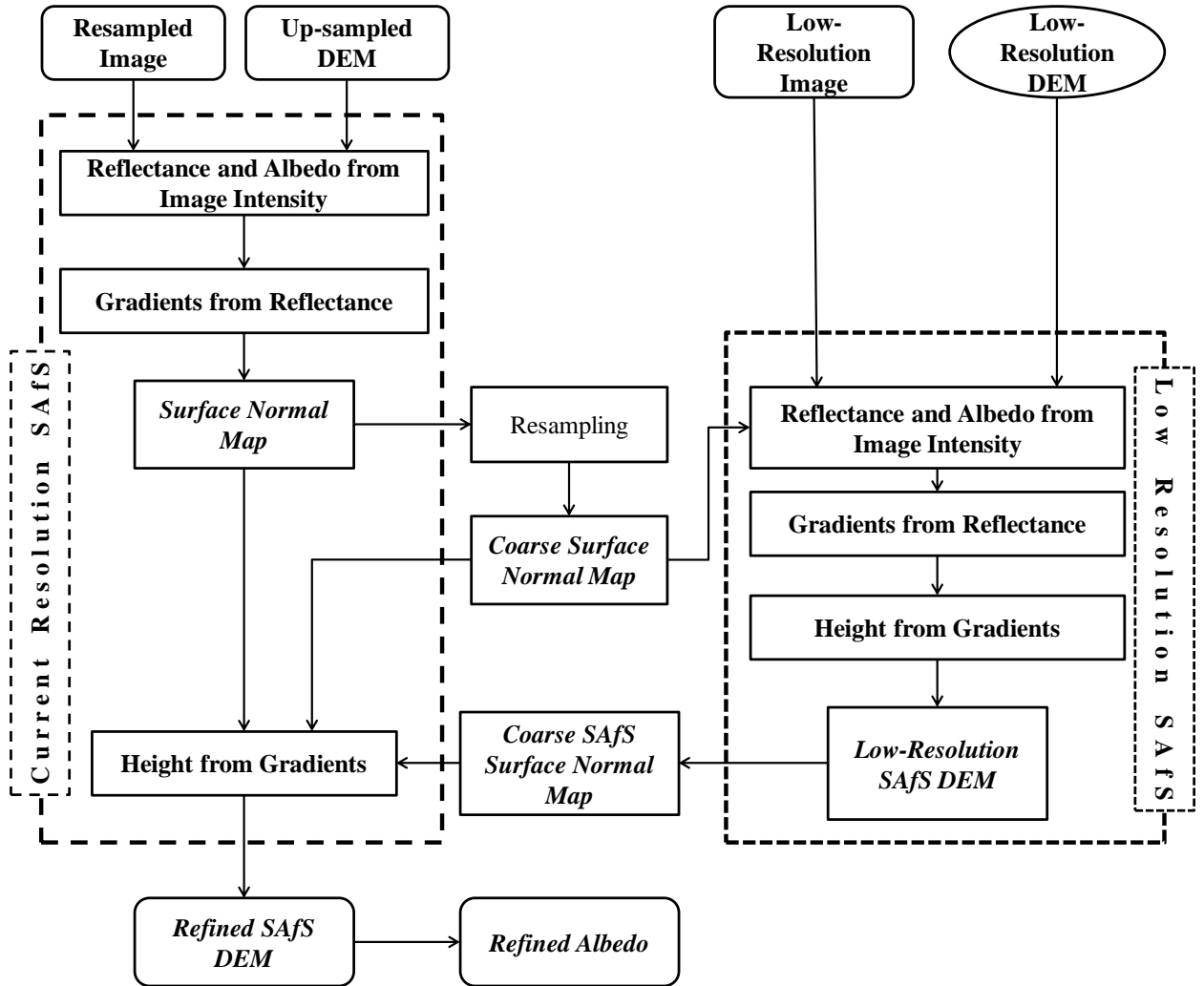


Fig. 3 Workflow of the multiple-grid SAfS algorithm.

4. Experimental Analysis

4.1 Datasets

Three experimental datasets were presented and analyzed in this study. The experimental analysis of the aforementioned SAFS algorithm uses the LRO NAC images as the input images. The LRO NAC images are characterized by their high resolution (0.5 - 1.5 m) and are able to provide very detailed lunar topography. The LRO NAC images were obtained from the LROC Archive (<http://lroc.sese.asu.edu/>) and ortho-rectified by the software program ISIS3 (<https://isis.astrogeology.usgs.gov/>). The specifications of the images are listed in Table 1.

Table 1. Details of LRO NAC imagery used in the experiments.

	Dataset 1	Dataset 2	Dataset 3
Image ID	M146255155	M104905963	M173246166
Resolution	1.5 m/pixel	1.5 m/pixel	0.5 m/pixel
Sun azimuth	90.31°	263.31°	151.95°
Approximated incidence angle	67.96°	49.16°	49.01°
Viewer azimuth	33.69°	271.16°	88.54°
Approximated emission angle	1.15°	11.76°	17.73°
Image dimension used in experiments	480 x 560 pixels	1520 x 1880 pixels	1320 x 1200 pixels

The SLDEM (Barker et al., 2015), a combined product of LOLA laser altimetry and the Japanese Selenological and Engineering Explorer (SELENE) terrain camera images, was

selected as the low-resolution DEM to provide constraint for SAfS. The SLDEM has a resolution of 60 m per grid, but it exhibits better geodetic accuracy and requires much less interpolation, which leads to fewer artifacts than the LOLA DEM. The SLDEM data were obtained from the PDS Geoscience Node (<http://pds-geosciences.wustl.edu/missions/lro/lola.htm>), and the images were aligned with the SLDEM during the ortho-rectification process.

High resolution DEMs (2 – 5 m resolution) available in the LROC Archive are used as independent reference DEMs for comparison analysis. These DEMs (referred to as NAC DEM) were derived from rigorous photogrammetric processing of stereo LRO NAC images. They have resolutions much higher than that of the SLDEM but lower than that of the image and are able to provide a direct comparison analysis of the SAfS DEMs; note that for dataset 1, there is no NAC DEM available from the LROC Archive.

4.2 Experimental Analysis for Dataset 1

Experimental dataset 1 covers a relatively smooth area, as revealed by Figures 4 and 5. A larger crater that spans approximately 3×3 cells on the SLDEM is clearly visible on the image (Figure 6b), but its geometry is not preserved in the SLDEM. The high sun elevation angle image (Figure 7b) shows that the area is covered by traces of the ejecta blanket of a larger impact nearby, which leads to drastic albedo changes. These albedo changes are almost absent in the input image (Figure 4), which implies that albedo recovery from the area would be challenging.

Figure 5 illustrates the three-dimensional view of the input SLDEM (Figure 5a) and the SAfS experimental result (Figure 5b). It is apparent that small details on the image are visible on the SAfS DEM, and the distinctive small craters at the upper right and lower left corners

of the area and the larger crater mentioned above are clearly recovered. Figure 6 compares two selected profiles with their counterparts on the SLDEM. Profile 1 (Figure 6a) shows the recovery of the larger crater as compared to the profile of the SLDEM, which is almost linear. The image of the feature enclosed in the dotted box was extracted (Figure 6b) and compared with the shaded relief of the same area (Figure 6c), which is a visual measurement of how much the details on the image are preserved in the SAfS DEM; they clearly show a high degree of correspondence with each other. Another profile (Figure 6e) shows the recovery of the distinctive small crater on the SAfS but not on the SLDEM. The crater has a sharp intensity contrast on its edge, which allows the rim to be reconstructed with the SAfS algorithm.

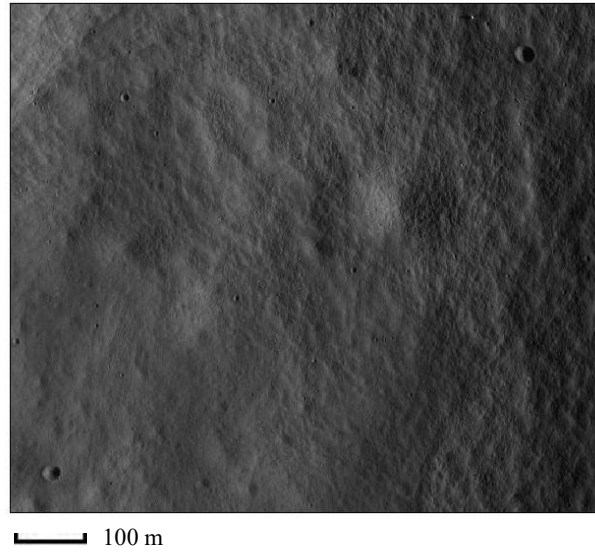


Fig. 4. Input image (1.5 m resolution) of experimental dataset 1.

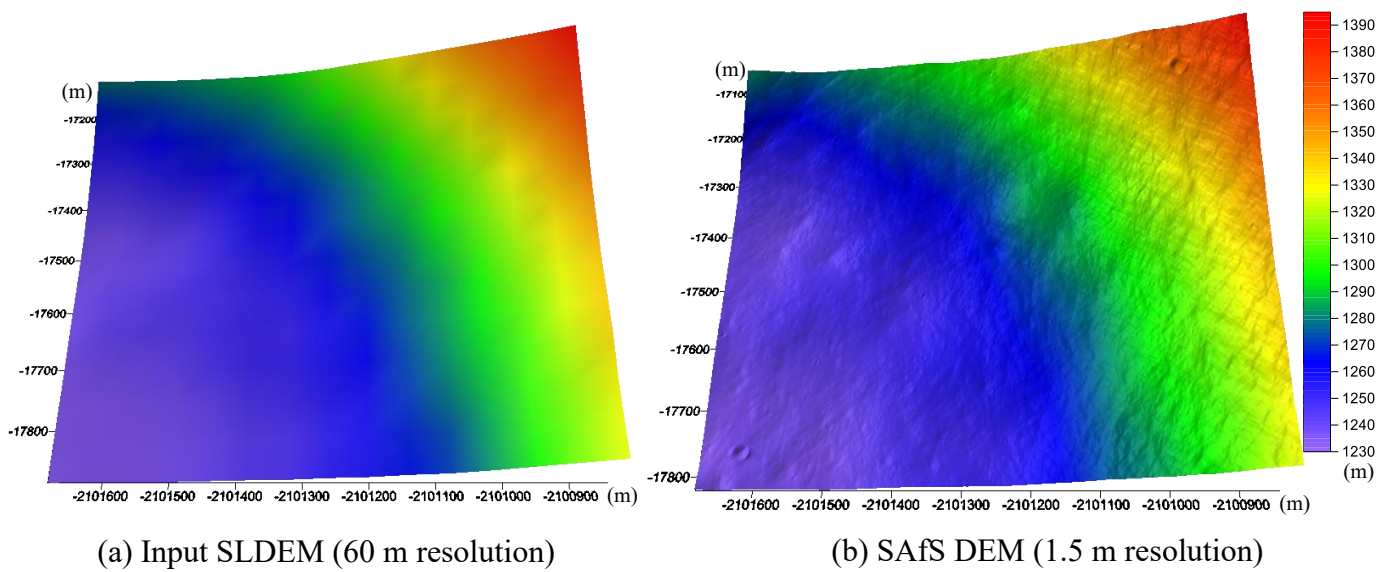
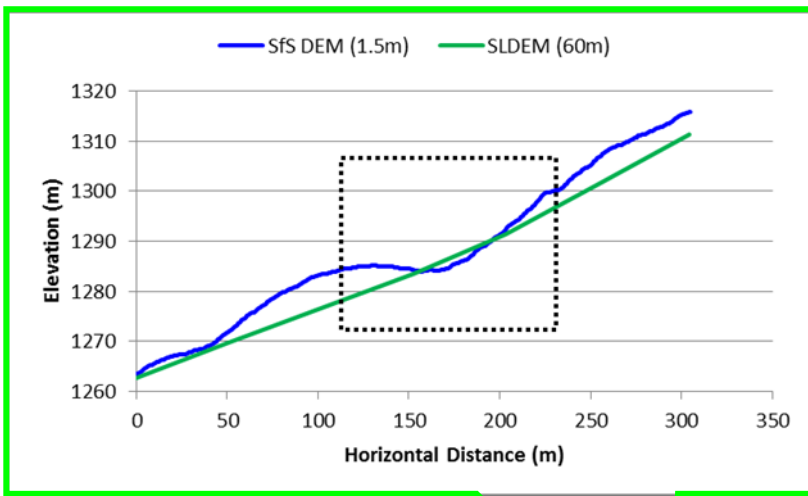
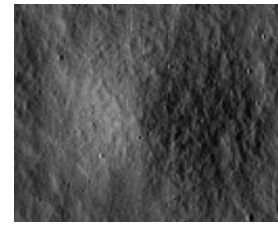


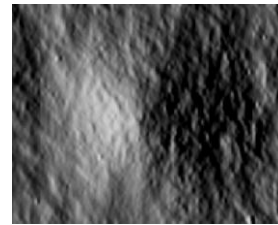
Fig. 5. 3D view of the input SLDEM and the output SAfS DEM (the two DEMs share the same color scale) of experimental dataset 1.



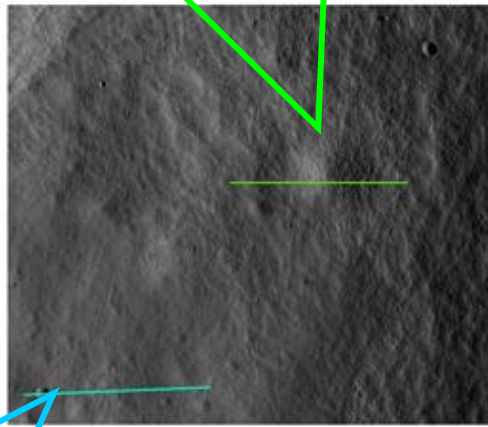
(a) Profile 1



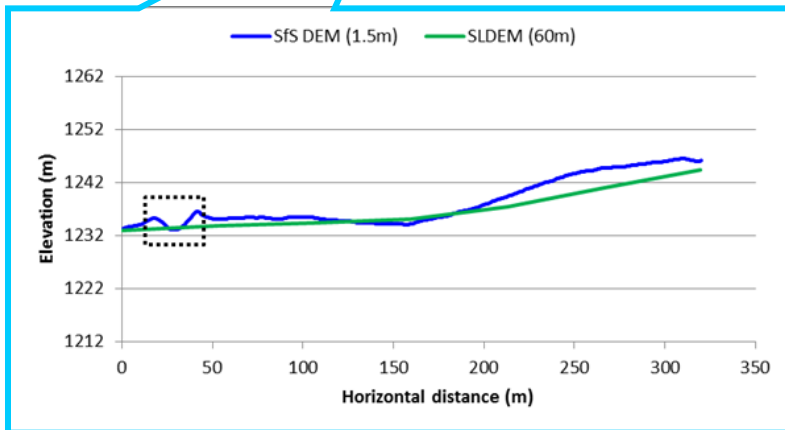
(b) Image



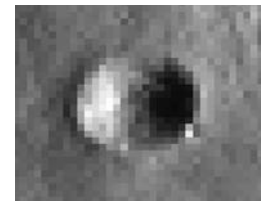
(c) Shaded relief of SFS DEM



(d) Location of profiles



(e) Profile 2



(f) Image



(g) Shaded relief of SFS DEM

Fig. 6. Profile and visual comparison for experimental dataset 1.

The albedo map derived from the SAfS results is presented in Figure 7 and compared to the high sun elevation angle imagery of the same area, because images with high sun elevation angles minimize the shading effects caused by terrain and highlight the local albedo changes. The derived albedo map has plausible correspondence with the high sun elevation angle image, especially the dark stripes at the lower left portion of the area. The albedo changes are largely covered by shading in the lower sun angle images required by the SAfS algorithm, and very few clues remain in such images, which makes it difficult to recover a reasonable albedo from monocular imagery.

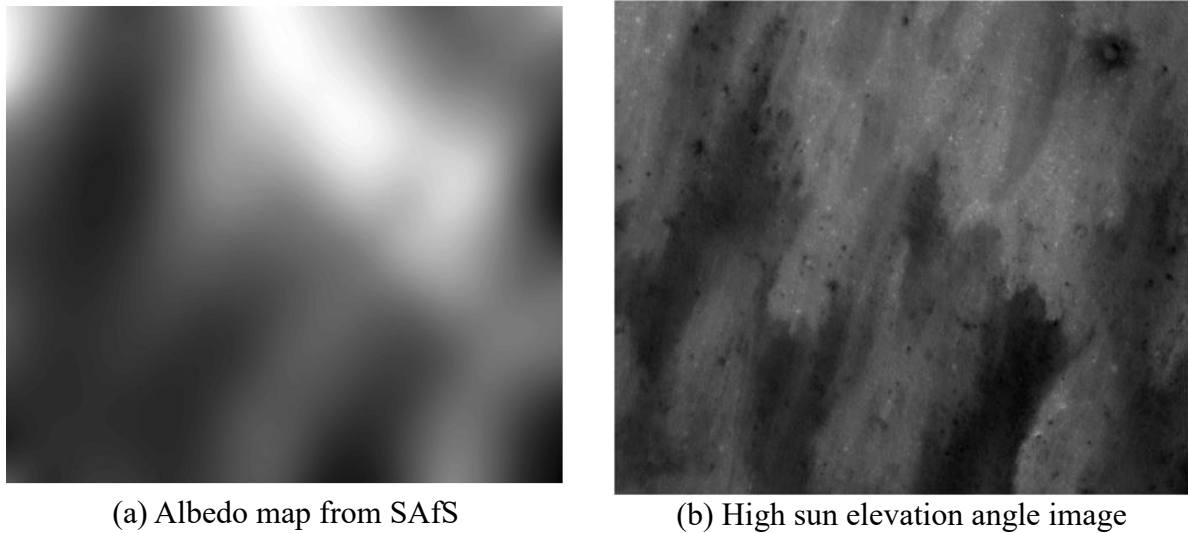


Fig. 7. Albedo comparison of experimental dataset 1.

4.3 Experimental Analysis for Dataset 2

Experimental dataset 2 shows a part of the Reiner Gamma area (Figure 8). Reiner Gamma is well known for the existence of lunar swirls (Denevi et al., 2016), which are patches of higher albedo on the lunar surface. With the presence of lunar swirls, experimental dataset 2 undergoes significant albedo changes even on a relatively flat area, which can be revealed by the rotated “Y” shape of the dark patch in the middle of Figure 11b. Choosing

this area helps to better understand the performance of SAfS from monocular imagery in a non-constant albedo area.

Figure 9 shows 3D views of the SLDEM, the SAfS result, and the reference NAC DEM (4.5 m resolution). The key geometry of the shape represented by the NAC DEM (Figure 9c) is well preserved in the SLDEM (Figure 9a), which allows the algorithm to converge to a result (Figure 9b) with high correspondence with the reference NAC DEM. The profile comparisons in Figure 10 demonstrate the consistency between the SAfS DEM and the reference NAC DEM, whereas very small details are recovered in the SAfS DEM, as shown by the shaded relief. The profiles have an absolute vertical root-mean-square error (RMSE) of 5 to 6 m with a maximum error of about 10 m as shown in Table 2; the larger residuals stem from the depth of the craters; the SAfS DEM, constrained by the input SLDEM, has shallower craters than the reference NAC DEM.

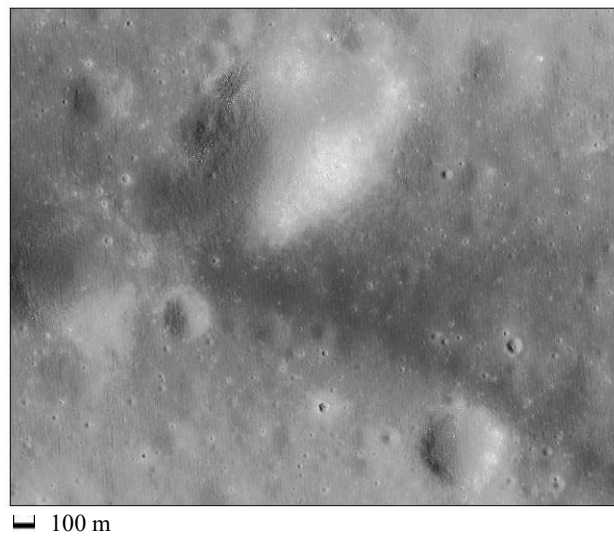
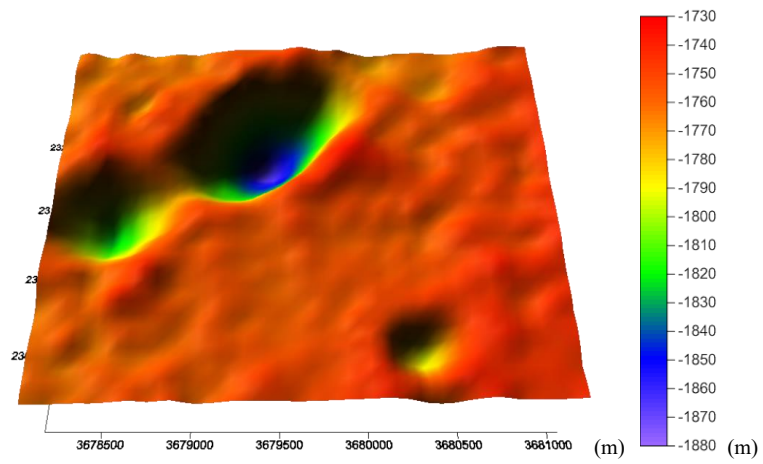
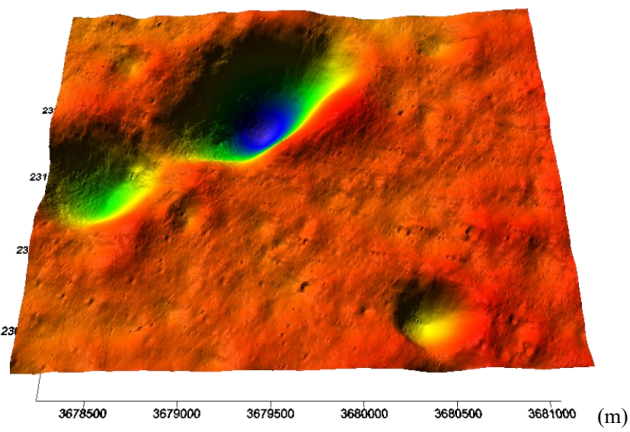


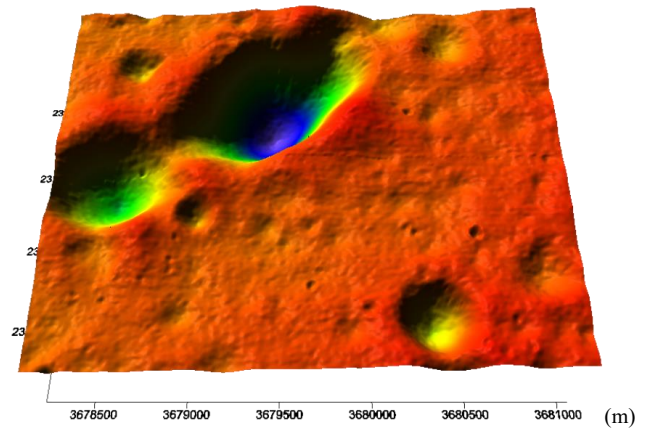
Fig. 8. Input image (1.5 m resolution) of experimental dataset 2.



(a) Input SLDEM (60 m resolution)

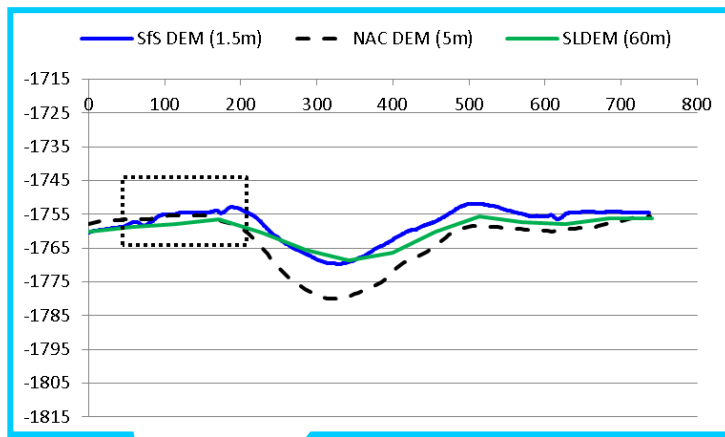


(b) SAfS DEM (1.5 m resolution)

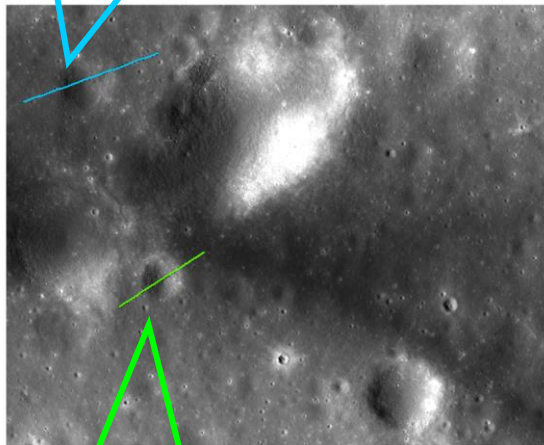


(c) Reference NAC DEM (4.5 m resolution)

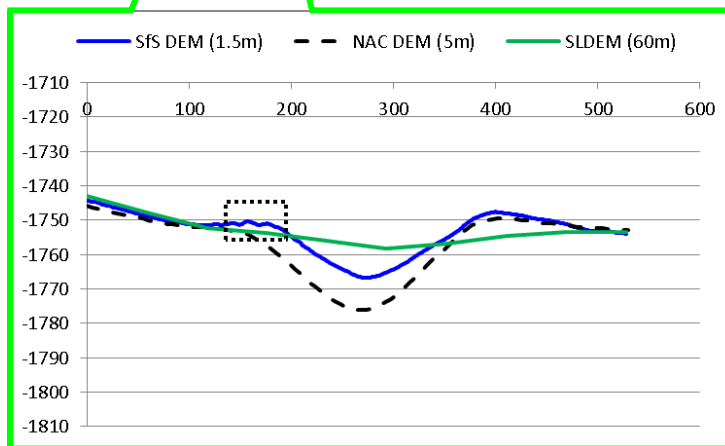
Fig. 9. 3D view of the input SLDEM, output SAfS DEM, and reference NAC DEM (the three DEMs share the same color scale) of experimental dataset 2.



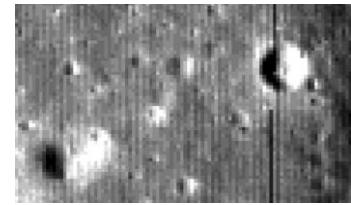
(a) Profile 1



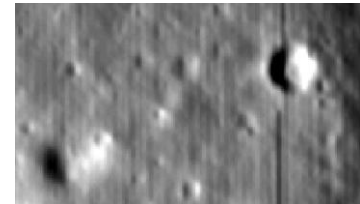
(e) Location of profiles



(f) Profile 2



(b) Image



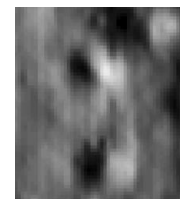
(c) Shaded relief of SFS DEM



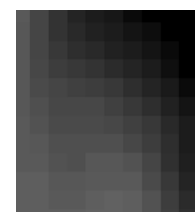
(d) Shaded relief of NAC DEM



(g) Image



(h) Shaded relief of SFS DEM



(i) Shaded relief of NAC DEM

Fig. 10. Profile and visual comparison for experimental dataset 2.

Table 2. Statistical analysis of profiles for experimental dataset 2.

	Mean (m)	RMSE (m)	Maximum absolute deviation (m)
Profile 1	1.04	6.34	11.19
Profile 2	3.42	4.94	10.08

The albedo of experimental dataset 2 is presented in Figure 11 and compared with the corresponding high sun elevation angle image. The comparison suggests promising albedo recovery where shading components are visually minimized in the albedo image, and the albedo changes caused by, for example, impact ejecta and lunar swirls are preserved in the albedo image. Stripes are visible on the recovered albedo aligned along the illumination direction, which is similar to the results obtained by Barron and Malik (2011) and Kirk et al. (2003). This may be explained by the physical nature of the SAfS, in which slopes along the illumination direction can be better estimated than slopes in the perpendicular direction.

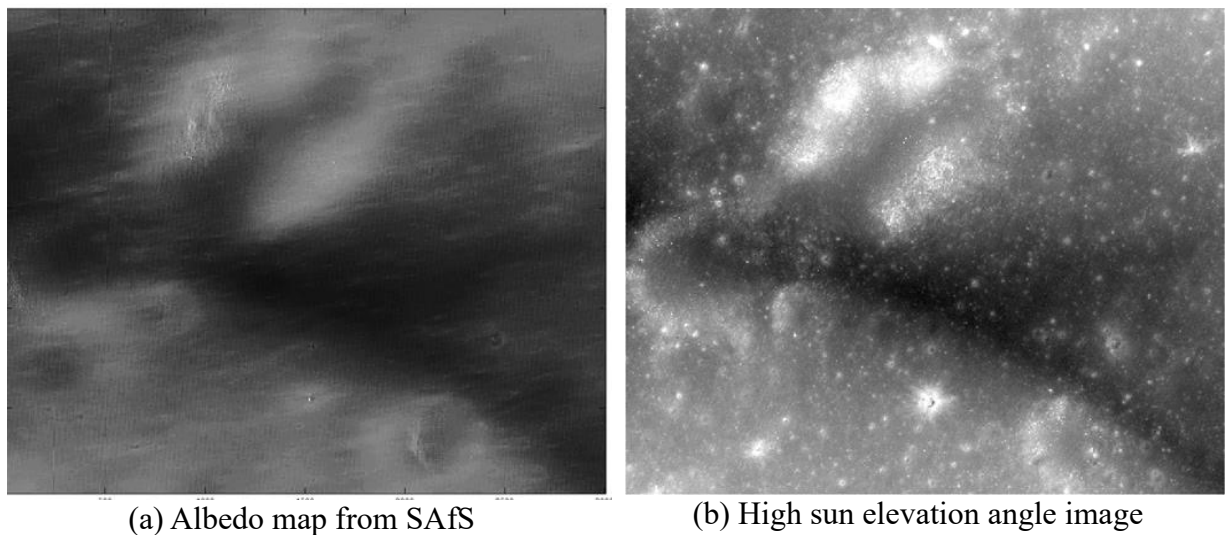


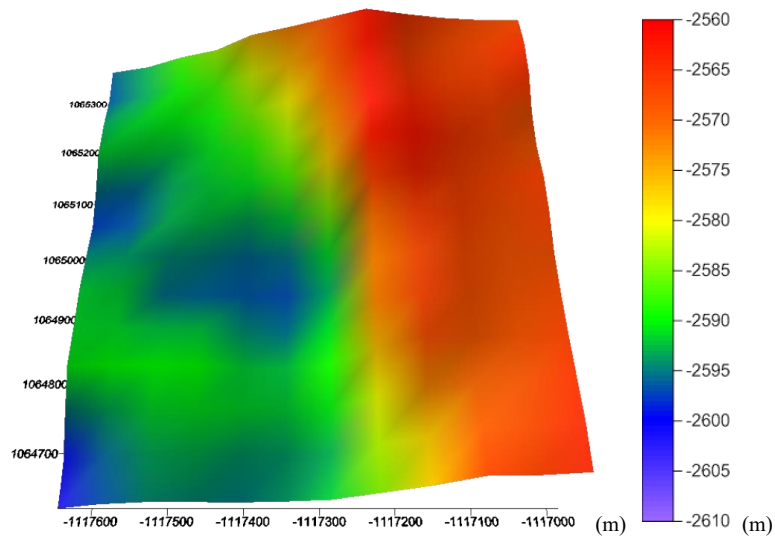
Fig. 11. Albedo comparison of experimental dataset 2.

4.4 Experimental Analysis for Dataset 3

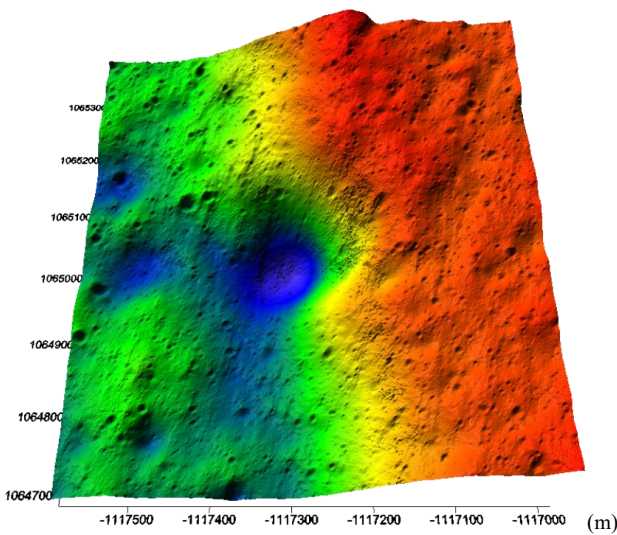
Experimental dataset 3 covers a large crater (about 300 m in diameter) located right on the edge of a rima (Figure 12); it exhibits significant height differences between the two sides of the crater, which increases the complexity and difficulty of recovery. From Figure 13a, it can be seen that the SLDEM does not preserve the overall geometry of the crater as well as the NAC DEM (spatial resolution, 1.5 m) in Figure 13c; therefore, part of the crater is not well recovered from SAfS, as indicated in the SAfS DEM in Figure 13b, although it reveals much more terrain detail than the NAC DEM cannot capture. Profile comparisons and the shaded relief in Figure 14 suggest that small boulders and craters are recovered. Table 3 shows the absolute vertical RMSE of the profiles. The residuals stem mainly from the unsatisfactory reconstruction of the crater (Figure 14f).



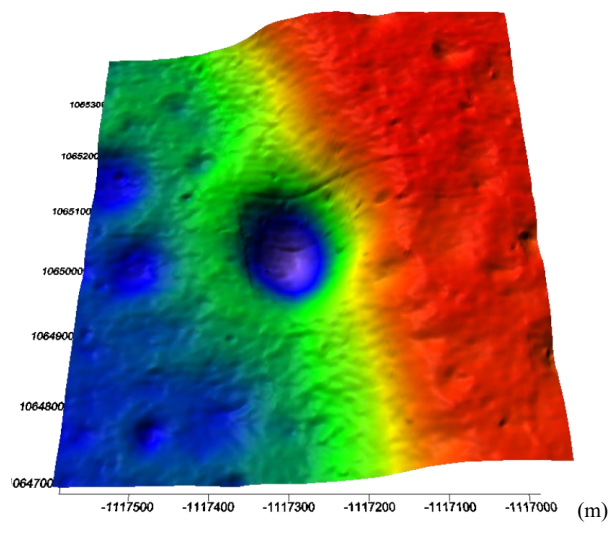
Fig. 12. Input image (0.5 m resolution) of experimental dataset 3.



(a) Input SLDEM (60 m resolution)

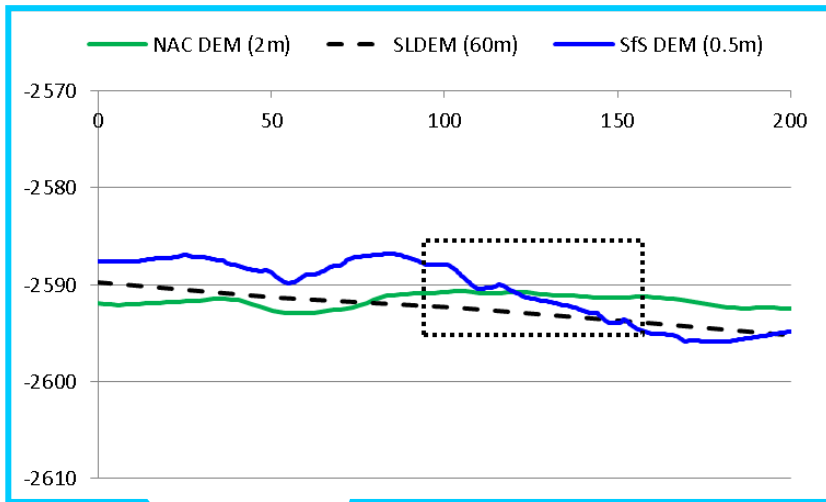


(b) SAfS DEM (0.5 m resolution)

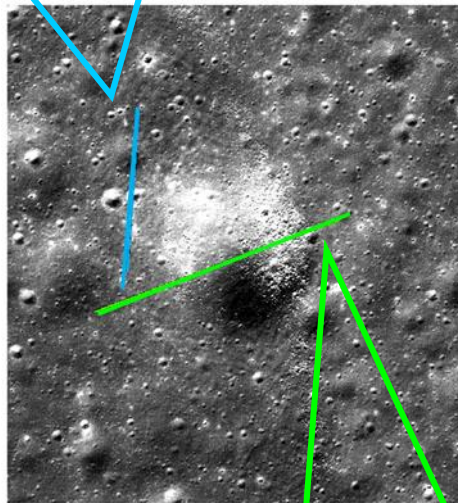


(c) Reference NAC DEM (2 m resolution)

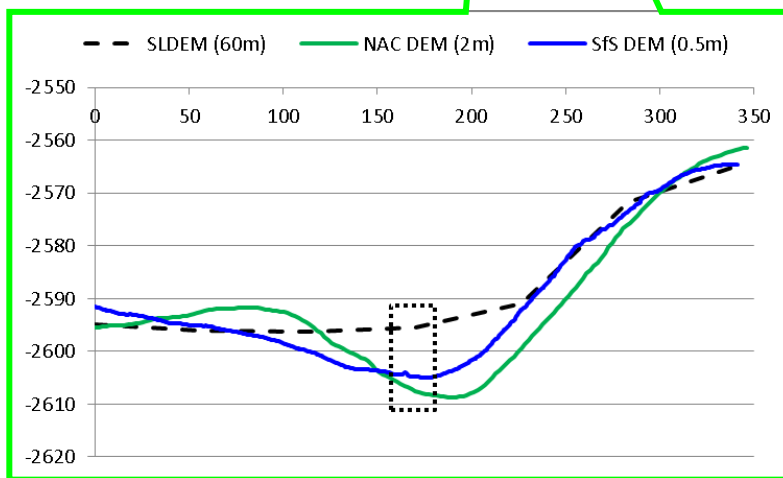
Fig. 13. 3D view of the input DEM, output SAfS DEM, and reference NAC DEM (the three DEMs share the same color scale) of experimental dataset 3.



(a) Profile 1



(e) Location of profiles



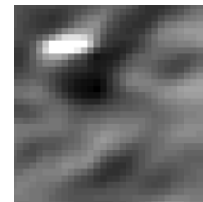
(f) Profile 2



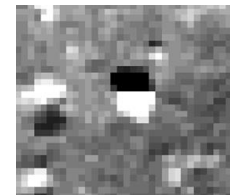
(b) Image



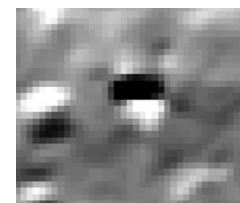
(c) Shaded relief of Sfs DEM



(d) Shaded relief of NAC DEM



(g) Image



(h) Shaded relief of Sfs DEM



(i) Shaded relief of NAC DEM

Fig. 14. Profile and visual comparison for experimental dataset 3.

Table 3. Statistical analysis of profiles for experimental dataset 3.

	Mean (m)	RMSE (m)	Maximum absolute deviation (m)
Profile 1	0.99	3.42	5.21
Profile 2	0.98	4.43	8.03

The general consistency between the SAFS DEM and the reference NAC DEM is visibly lower than for the previous two datasets, and two reasons for such inconsistency are identified.

The profiles in Figure 14 and 3D views of the input SLDEM and NAC DEM suggest that the input SLDEM cannot preserve the key geometry of the crater and the lower left portion of the area. The crater is represented by a flat slope in the SLDEM, whereas the lower left portion of the area has a higher elevation in the SLDEM than in the reference NAC DEM. This is similar to the cases in experimental dataset 1 (Figure 6a) and dataset 2 (Figure 10f); however, due to the complex geometry of the crater vicinity, reconstruction of the rim becomes difficult.

A profile along the direction perpendicular to illumination is extracted, and the intensity values of the image and the shaded NAC DEM are compared in Figure 15. The shaded NAC DEM profile, as shown by the upper green line in Figure 15b, shows a significant decrease in intensity at the edge of the crater, whereas the image intensity (blue line) shows no visible change. This suggests an albedo increase in the crater area and that insufficient information content has been captured in the image or in the input SLDEM. Therefore, the monocular imagery SAFS algorithm does not have sufficient information to estimate an accurate reflectance and its subsequent shape.

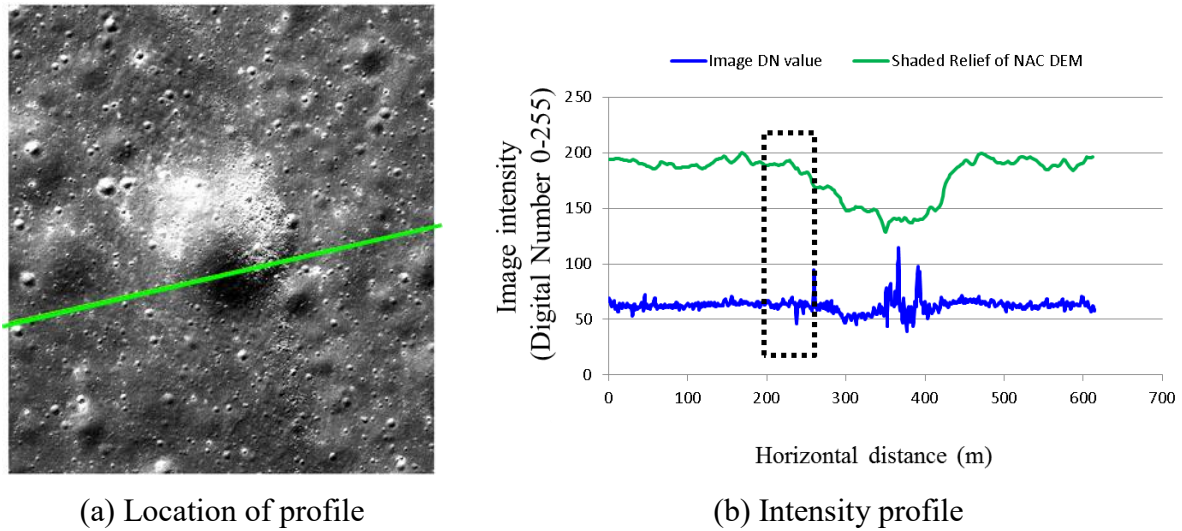
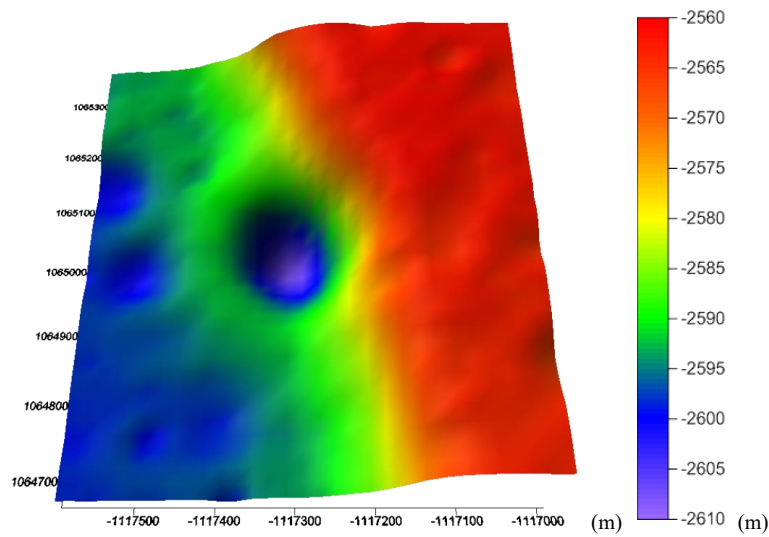


Fig. 15. Intensity profile of experimental dataset 3.

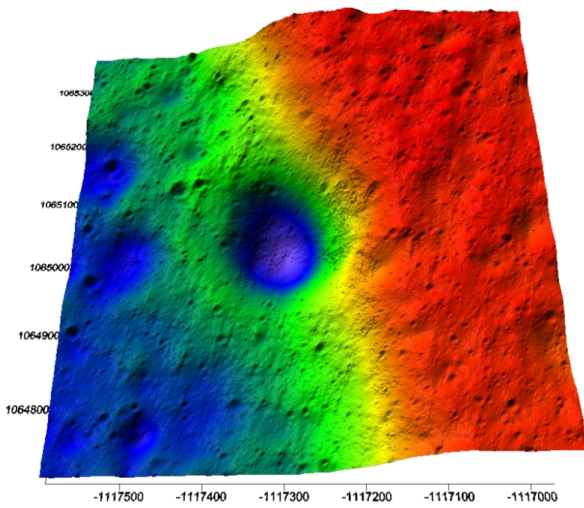
The second reason is an albedo issue. Because it cannot be correctly solved with a single image, the geometric control of the algorithm can be increased by using a better input DEM. To verify this assumption, the NAC DEM was down-sampled to 20 m per pixel and used as the input DEM (Figure 16a), such that the new input DEM possesses better properties in terms of resolution and preservation of geometry than the previous SLDEM in Figure 13a. The SAfS result (Figure 16b) produces a much better DEM with preservation of the details on the image and a high degree of consistency with the reference NAC DEM. This shows a good example of solution uniqueness as mentioned by Horn (1990); the algorithm may converge to a different solution (Figure 13b and Figure 16b), whereas the image details are almost equally preserved in the resulting DEM.

Profile comparisons and the shaded reliefs in Figure 17 show that the SAfS DEM constrained by a better input DEM also reconstructs very small boulders and craters. Comparing profile 1 of the new result (Figure 17a) with the old result (Figure 14a) illustrates an example of the influence of the quality of the input DEM. In the old profile in Figure 14a, the SAfS DEM is following the SLDEM with its profile tilted slightly to the right, whereas it becomes generally horizontal in the new profile in Figure 17a because its input DEM

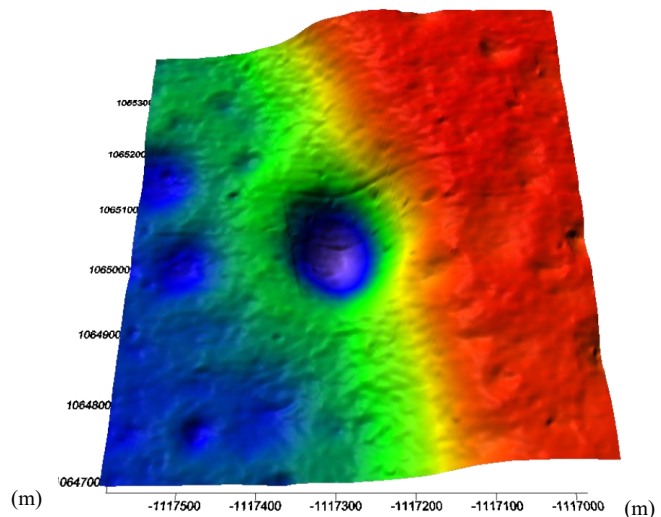
possesses a horizontal profile. The absolute vertical RMSE of the profiles as concluded in Table 4 also improves to less than 2 m, with a maximum of less than 4 m. The shaded reliefs shown in Figure 17 and Figure 14 also indicate that the shaded SAfS DEM with SLDEM as the input is brighter than that with the 20-m NAC DEM as the input, which implies that the former DEM is more sunward-facing than the latter.



(a) Down-sampled 20-m NAC DEM used as input

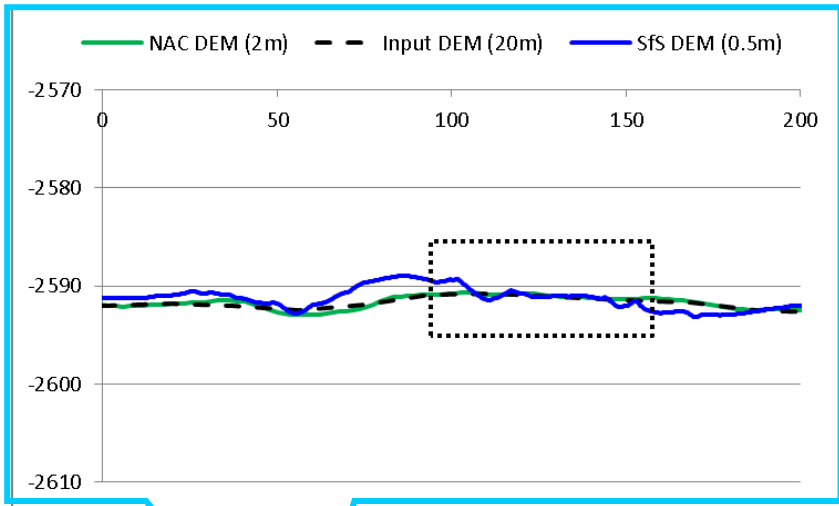


(b) SAfS DEM (0.5 m resolution)

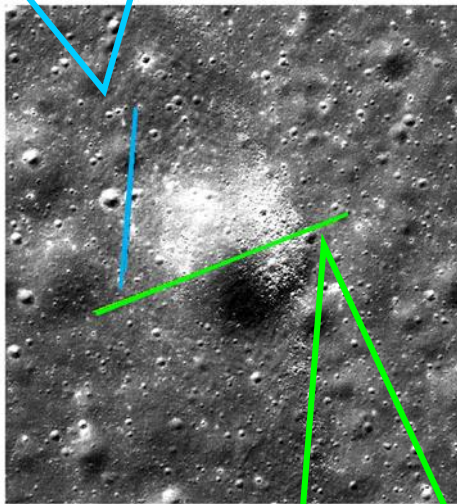


(c) Reference NAC DEM (2 m resolution)

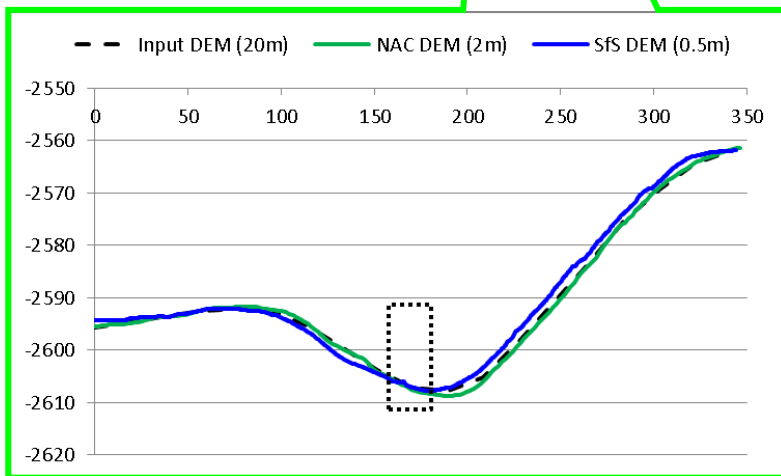
Fig. 16. 3D view of the input DEM (20-m NAC DEM), output SAfS DEM, and reference NAC DEM (the three DEMs share the same color scale) of experimental dataset 3.



(a) Profile 1



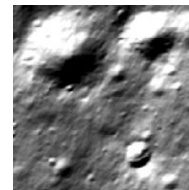
(e) Location of profiles



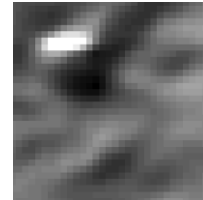
(f) Profile 2



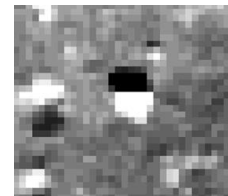
(b) Image



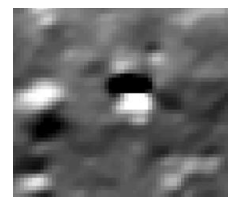
(c) Shaded relief of Sfs DEM



(d) Shaded relief of NAC DEM



(g) Image



(h) Shaded relief of Sfs DEM



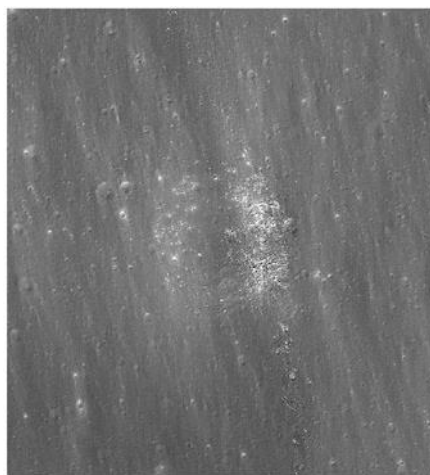
(i) Shaded relief of NAC DEM

Fig. 17. Profile and visual comparison for experimental dataset 3 with the 20-m input DEM.

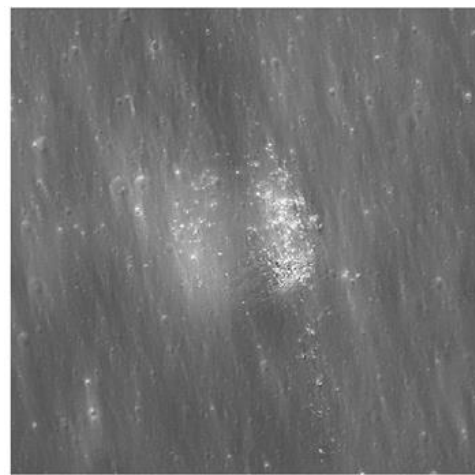
Table 4. Statistical analysis of profiles for experimental dataset 3 constrained by the down-sampled 20-m NAC DEM.

	Mean (m)	RMSE (m)	Maximum absolute deviation (m)
Profile 1	0.41	1.06	2.63
Profile 2	0.85	1.85	3.80

The albedo images of both results are presented and compared in Figure 18. The albedo image constrained by the higher-resolution input DEM (Figure 18b) is apparently brighter in the crater area than that constrained by the SLDEM, which the image intensity in Figure 15 is unable to capture. Although the albedo image constrained by the SLDEM is also brighter in the crater area, its boundary is less distinctive than its counterpart, which implies a smoother shape in those boundaries. Both albedo images possess stripe artifacts along the illumination direction, which are similar to those discussed in experimental dataset 2.



(a) SAfS constrained by SLDEM

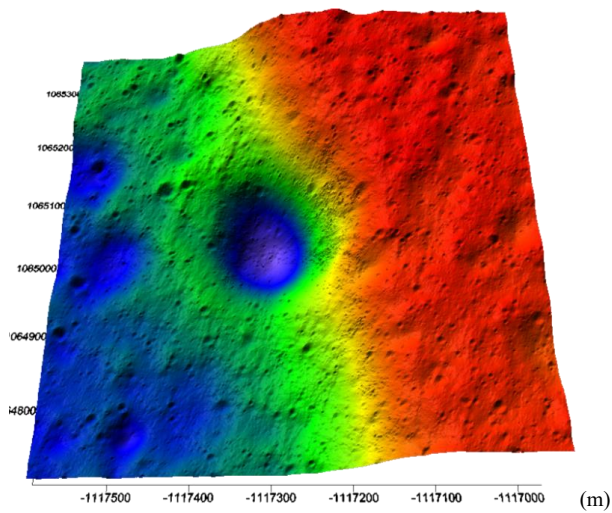


(b) SAfS constrained by 20-m NAC DEM

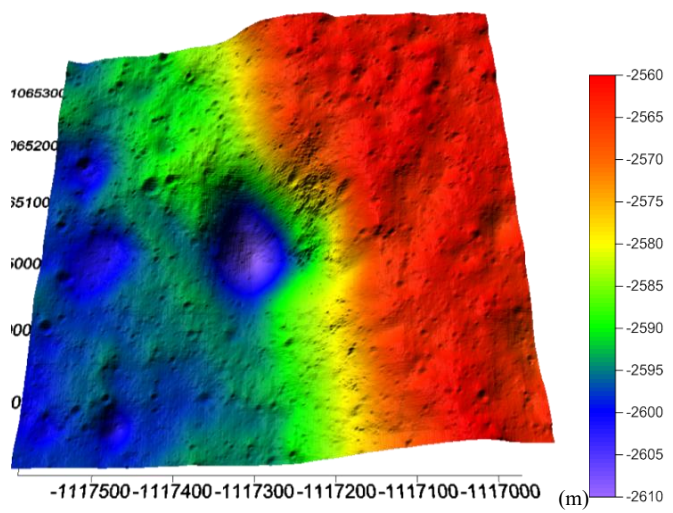
Fig. 18. Albedo comparison of experimental dataset 3.

To further examine the performance of the proposed SAfS approach, a DEM generated by the SfS approach presented by Grumpe et al. (2014) using the NAC image of experimental dataset 3 (referred as Grumpe et al. (2014)'s DEM) was involved for a detailed comparison analysis. Figure 19 a and b show a side-by-side comparison of the two DEMs, both show satisfactory details. The SAfS DEM generated by our approach (Figure 19a) preserves better geometry especially at the crater rim while Grumpe et al. (2014)'s DEM (Figure 19b) shows clear defects for the south-west part of the crater rim.

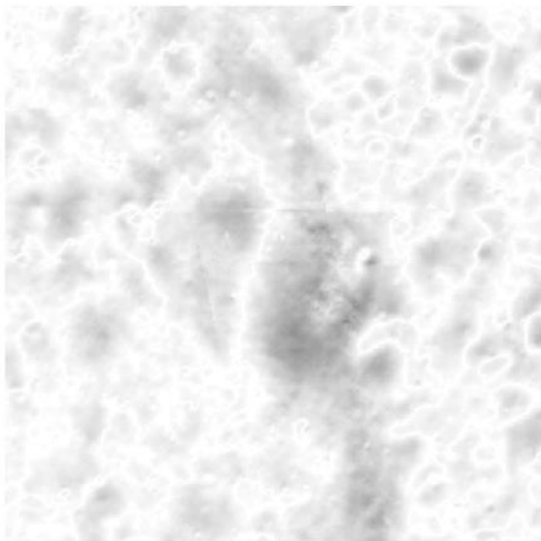
To quantitatively evaluate the DEM accuracies, our SAfS DEM and Grumpe et al. (2014)'s DEM were down-sampled to the same resolution of the reference NAC DEM, and difference DEMs were obtained by directly comparing them with the reference NAC DEM as shown in Figure 19 c and d. It is apparent that our SAfS DEM shows higher consistency with the independent reference NAC DEM. The difference DEM between Grumpe et al. (2014)'s DEM and the reference NAC DEM shows overall darker (larger inconsistency) values, especially at the crater and its nearby region. Table 5 summarizes the statistics of the two difference DEMs. Our SAfS DEM has a mean absolute error of 0.73 m and a maximum error of 4.44 m, while Grumpe et al. (2014)'s DEM has a mean absolute error of 1.23 m with an a maximum error of 10.19 m. This indicates the superior performance of the proposed SAfS approach.



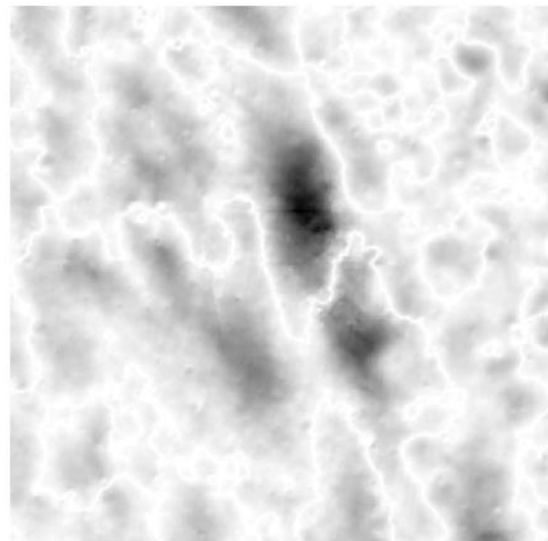
(a) SAfS DEM (0.5 m resolution) generated by our approach



(b) Grumpe et al. (2014)'s DEM (0.5 m resolution)



(c) Difference DEM between our SAfS DEM and the reference NAC DEM



(d) Difference DEM between Grumpe et al. (2014)'s DEM and the reference NAC DEM

Fig. 19. The SAfS DEM, Grumpe et al. (2014)'s DEM, and their comparison with the reference NAC DEM

Table 5. Statistics of the difference DEMs for experimental dataset 3.

	Difference DEM between the SAfS DEM and reference NAC DEM	Difference DEM between Grumpe et al. (2014)'s DEM and reference NAC DEM
Mean absolute deviation (m)	0.73	1.23
Maximum absolute deviation(m)	4.44	10.19

5. Conclusions and Discussion

This paper presents a SAfS algorithm to generate pixel-level resolution DEM and albedo maps from monocular imagery constrained by an existing low-resolution DEM. On the basis of experimental validation, it can be concluded that the SAfS algorithm is able to create pixel-level resolution DEMs that preserves the details visible in the image (0.5 - 1.5 m resolution) while keeping the overall geometry consistent with the low-resolution DEM used as a constraint. The experimental analysis achieved an absolute vertical RMSE of not more than 7 m and a maximum of approximately 10 m. The reconstructed albedo shows a high degree of correspondence with high sun elevation angle images, which serve as references of albedo changes, implying that the albedo information embedded in the image is satisfactorily estimated and separated from shading by the SAfS algorithm.

Experimental analysis 3 highlights the dependency of the SAfS result on the quality of the input low-resolution DEM, and especially on whether the key geometry is preserved in the low-resolution DEM for its effective resolution. The algorithm's albedo estimation method smooths out the boundaries of actual drastic albedo changes; therefore, if the resolution difference between the image and the constraining DEM is too large, it will create greater ambiguity for the solution, which may lead to inaccuracies in shape and albedo. In

this case, an input DEM with better properties such as geometry preservation and resolution would be preferred to increase the reliability for detailed shape recovery.

Currently, only the reflectance of the image and a low-resolution DEM are used in the SAfS. More clues can be obtained from images through techniques such as image manipulation and image statistics, which are well-developed in the domain of image analysis and computer vision. It should be possible to integrate these techniques into the SAfS algorithm in a future study.

Acknowledgments

This work was supported by a grant from the Research Grants Council of Hong Kong (Project No. PolyU 152086/15E), grants from the National Natural Science Foundation of China (Project No. 41471345 and Project No. 91338110), and a grant from the China Academy of Space Technology (Contract No. 15CPC/HK0201). The authors thank all those who worked on the Planetary Data System archive to make the LROC imagery and SLDEM publicly available.

References

1. Barker, M. K., Mazarico, E., Neumann, G. A., Zuber, M. T., Haruyama, J., Smith, D. E., 2015. A new lunar digital elevation model from the Lunar Orbiter Laser Altimeter and SELENE Terrain Camera. *Icarus*, 273(2016): 346-355.
2. Barron, J. T., Malik, J., 2011. High-frequency shape and albedo from shading using natural image statistics. 2011 IEEE Conference on Computer Vision and Pattern Recognition, Colorado Springs, CO, USA, pp. 2521-2528.

3. Barron, J. T., Malik, J., 2012. Shape, albedo, and illumination from a single image of an unknown object. Proceedings of the IEEE Conference on Computer Vision and Pattern Recognition, Providence, RI, USA.
4. Chandraker, M., Agarwal, S., Kriegman, D., 2007. ShadowCuts: Photometric Stereo with Shadows. Proceedings of the IEEE Conference on Computer Vision and Pattern Recognition, Minneapolis, MN, USA.
5. Danzl, R., Scherer, S., 2002. Integrating shape from shading and shape from stereo for variable reflectance surface reconstruction from SEM images. Proceedings of 26th Workshop of the Austrian Association for Pattern Recognition: 281-288.
6. Denevi, B. W., Robinson, M. S., Boyd, A. K., Blewett, D. T., Klima, R. L., 2016. The distribution and extent of lunar swirls. *Icarus*, 273(2016): 53-67.
7. Frankot, R. T., Chellappa, R., 1988. A method for enforcing integrability in shape from shading algorithms. *IEEE Transactions on Pattern Analysis and Machine Intelligence*, 10(4): 439-451.
8. Grumpe, A., Belkhir, F., Wöhler, C., 2014. Construction of lunar DEMs based on reflectance modelling. *Advances in Space Research*, 53: 1735-1767.
9. Hapke, B., 2002. Bidirectional reflectance spectroscopy. 5: The coherent backscatter opposition effect and anisotropic scattering. *Icarus*, 157(2): 523-534.
10. Hapke, B., 2012. *Theory of Reflectance and Emittance Spectroscopy*. 2nd edition. Cambridge University Press, Cambridge, UK.
11. Hashemi, L., Azizi, A., Hashemi, M. H., 2002. Implementation of a single photo shape from shading method for the automatic DTM generation. *International Archives of Photogrammetry and Remote Sensing*, 34(B3): 71-74.
12. Horn, B. K. P., 1977. Understanding image intensities. *Artificial Intelligence*, 8(2): 201-231.

13. Horn, B. K. P., 1990. Height and gradient from shading. *International Journal of Computer Vision*, 5(1): 37-75.
14. Kirk, R. L., Barrett, J. M., Soderblom, L. A., 2003. Photoclinometry made simple...? ISPRS Commission IV, Working Group IV/9, "Advances in Planetary Mapping" Workshop, Houston, TX.
15. Lee, C.-H., Rosenfeld, A., 1983. Albedo estimation for scene segmentation. *Pattern Recognition Letters*, 1(3): 155-160.
16. Lohse, V., Heipke, C., 2004. Multi-image shape-from-shading: Derivation of planetary digital terrain models using Clementine images. *International Archives of Photogrammetry and Remote Sensing*, 35(B4): 828-833.
17. Lohse, V., Heipke, C., Kirk, R. L., 2006. Derivation of planetary topography using multi-image shape-from-shading. *Planetary and Space Science*, 54(2006):661-674.
18. Maxwell, B. F., 2005. Planetary photometry: The Lommel-Seeliger law. *Journal of the Royal Astronomical Society of Canada*, 99(3): 92-93.
19. McEwen, A.S., 1991. Photometric functions for photoclinometry and other applications. *Icarus*, 92(2): 298-311.
20. Piechullek, C., Heipke, C., 1996. DTM refinement using multi image shape from shading. *International Archives of Photogrammetry and Remote Sensing*, 31(B3): 644-651.
21. Piechullek, C., Heipke, C., Ebner, H., 1998. Multi image shape from shading: Results using real aerial imagery. *International Archives of Photogrammetry and Remote Sensing*, 32(3/1): 160-167.
22. Smith, D. E., Zuber, M. T., Jackson, G. B., Cavanaugh, J. F., Neumann, G. A., Riris, H., Sun, X., Zellar, R. S., Coltharp, C., Connelly, J., Katz, R. B., Kleyner, I., Liiva, P., Matuszeski, A., Mazarico, E. M., McGarry, J. F., Novo-Gradac, A.-M., Ott, M. N., Peters, C., Ramos-Izquierdo, L. A., Ramsey, L., Rowlands, D. D., Schmidt, S., Scott, V. S. III,

- Shaw, G. B., Smith, J. C., Swinski, J.-P., Torrence, M. H., Unger, G., Yu, A. W., Zagwodzki, T. W., 2010. The lunar orbiter laser altimeter investigation on the lunar reconnaissance orbiter mission. *Space Science Reviews*, 150: 209-241.
23. Tran, T., Rosiek, M. R., Beyer, R. A., Mattson, S., Howington-Kraus, E., Robinson, M. S., Archinal, B. A., Edmundson, K., Harbour, D., Anderson, E., the LROC Science Team, 2010. Generating digital terrain models using LROC NAC images. A special joint symposium of ISPRS Technical Commission IV & AutoCarto in conjunction with ASPRS/CaGIS, Orlando, FL.
24. Tsai, P.-S., Shah, M., 1998. Shape from shading with variable albedo. *Optical Engineering*, 37(4): 1212-1220.
25. Wang, T. C., Chandraker, M., Efros, A. A., Ramamoorthi, R., 2016. SVBRDF-Invariant Shape and Reflectance Estimation from Light-Field Cameras. *Proceedings of the IEEE Conference on Computer Vision and Pattern Recognition*, Las Vegas, NV, USA.
26. Woodham, R., 1980. Photometric method for determining surface orientation from multiple images. *Optical Engineering*, 19(1): 139-144.
27. Wu, B., Li, F., Ye, L., Qiao, S., Huang, J., Wu, X., Zhang, H., 2014a. Topographic modeling and analysis of the landing site of Chang'E-3 on the moon. *Earth and Planetary Science Letters*, 405(2014): 257-273.
28. Wu, B., Hu, H., Guo, J., 2014b. Integration of Chang'E-2 Imagery and LRO Laser Altimeter Data with a Combined Block Adjustment for Precision Lunar Topographic Modeling. *Earth and Planetary Science Letters*, 391 (2014): 1–15.
29. Zhu, Q., Zhang, Y., Wu, B., Zhang, Y., 2010. Multiple close-range image matching based on a self-adaptive triangle constraint. *Photogrammetric Record*, 25(132): 437-453.